Thermoelectric transport properties of $CuFeInTe_3$

H. Cabrera [a,b,*], I. Zumeta-Dubé [c], D. Korte [d], P. Grima-Gallardo [e], F. Alvarado [e], J. Aitken [f], J.A. Brant [f], J.H. Zhang [f], A. Calderón [c], E. Marín [c], M. Aguilar-Frutis [c], J. E. Erazo [e], E. Perez-Cappe [g] and M. Franko [d]

[a] SPIE-ICTP Anchor Research Laboratory, International Centre for Theoretical Physics (ICTP), Strada Costiera 11, Trieste, Italy.
[b] Centro Multidisciplinario de Ciencias, Instituto Venezolano de Investigaciones Científicas (IVIC),Mérida 5101, Venezuela.
[c] Instituto Politécnico Nacional, Centro de Investigación en Ciencia Aplicada y Tecnología Avanzada, Unidad Legaria, México D.F. 11500, México.

[d] University of Nova Gorica, Laboratory for Environmental Research, Vipavska 13, 5000 Nova Gorica, Slovenia.
[e] Centro de Estudios en Semiconductores (CES). Dpto. Física. Fac. Ciencias. Universidad de Los Andes. Mérida. Venezuela.
[f] Department of Chemistry and Biochemistry. Duquesne University. Pittsburgh, USA.
[g] Instituto de Ciencia y Tecnología de Materiales (IMRE, Universidad de La Habana,Vedado, Cuba

*Electronic mail corresponding author: hcabrera@ictp.it

ABSTRACT

In this paper we report on the preparation of $CuFeInTe_3$ and its thermoelectric properties. Optical diffuse reflectance and Raman scattering spectroscopies, as well as X-ray powder diffraction were also carried out. Unprecedented for $CuFeInTe_3$, a direct and an indirect bang gap were found from its absorption spectrum. From Hall effect measurements at 300 K the carrier concentration (n), electrical conductivity (σ) and mobility (μ) were determined. In order to investigate whether this material is suitable for thermoelectric applications, the Seebeck coefficient (S), the thermal conductivity (κ) and σ as a function of temperature were measured. The measurements of Hall and Seebeck coefficients showed that alloying $CuInTe_2$ with Fe^{2+} produces a change from the original p-type to n-type conductivity and causes a decrease in κ value, while leaving σ unchanged. Relatively large S values were found for $CuFeInTe_3$, with respect to $CuInTe_2$, which were explained on the basis of a probable electron effective mass increase due to Fe^{2+} incorporation. It was also found, that thermal and electrical conductivities decrease with increasing temperature in the range between 300 and 450 K, while the figure of merit (zT) reaches values of 0.075 and 0.126 at 300 and 450 K respectively. Thus, zT of $CuFeInTe_3$ increases with temperature, reaching values larger than those reported for $CuInTe_2$.

1. Introduction

Semiconductors, due the unique thermal, optical and electronic properties, are used for many applications in electronic and optoelectronic devices. Among the physical parameters of interest, the electric properties (electrical conductivity, carrier concentration) determine the efficiency of the devices, whereas the thermal transport properties are of great importance for the lifetime of the electronic circuits.

Among all the semiconductors, the thermoelectric (TE) materials have attracted extensive attention because of their potential applications in heat pumping and power generation devices. The performance of TE materials is optimized by maximizing the dimensionless thermoelectric figure of merit:

$$zT = S^2 \sigma T / \kappa, \tag{1}$$

where S is the Seebeck coefficient, σ is the electrical conductivity, T is the absolute temperature and κ is the thermal conductivity [1-3]. The strategy of maximizing zT is to simultaneously obtain large power factors ($S^2\sigma$) as well as a low thermal conductivity.

A great variety of TE materials, such as Bi_2Te_3, PbTe, Cu_2S, Cu_2Se, skutterudites and clathrates [4-9], have been extensively studied. Despite that, the search for novel, high efficiency and cheaper materials is always open. In the last years, a family of compounds with diamond-like structure, the so called Te-based chalcopyrites have emerged as promised TE materials [10]. Among them, $CuInTe_2$, which is a well-known ternary chalcopyrite semiconductor, has received special attention due to its good electrical properties and low thermal conductivity. It is a ternary I–III–VI_2 compound with a direct band gap of approximately 1.02 eV [11]. The zT value of $CuInTe_2$ reaches 1.18 at 850 K, which is better than that of any other un-doped diamond-like material [12]. Moreover, for the $CuIn_{1-x}Cd_xTe_2$ alloys ($x = 0$, 0.02, 0.05, and 0.1) prepared by the melt-annealing method, the zT values are improved by over 100% at room temperature and ~20% at 600 K for $x = 0.02$ and 0.1, due to the substitution of Cd at In sites; thus, significantly increasing the carrier concentration as well as both the electrical conductivity and the power factor. Furthermore, the thermal conductivity is reduced by the presence of extra phonon scattering due to the difference in values of atomic mass and radius between Cd and In atoms [13]. It was also reported, that $(CuInTe_2)_{1-x}(ZnTe)_x$ alloys (simultaneous Zn substitution for both Cu and In) have a lower thermal conductivity, and attained a zT value of 0.69 at 737 K, which is 1.65 times higher than the zT value of Zn-free $CuInTe_2$ [14]. All these experimental results give encouragement to continue the investigation of $CuInTe_2$ alloys in the search for promising TE materials.

$CuFeInTe_3$ is a magnetic semiconductor belonging to the more general family of $(CuInTe_2)_{1-x}(FeTe)_x$ alloys with $x = 0.5$, which have been intensively studied for spintronic applications. Some of their structural, magnetic and thermal properties have been previously reported [15-17], while their thermoelectric properties have not been investigated. This paper focuses on the investigation of the thermoelectric properties of the $CuFeInTe_3$-alloy. This study was aided by Hall and Seebeck effect measurements, optical and Raman scattering spectroscopies and X-ray powder diffraction. In order to investigate whether this material is suitable for thermoelectric applications, we also calculated the thermoelectric figure of merit from the Seebeck coefficient and the thermal and the electrical conductivity measured as a function of temperature.

2. Experimental procedure

2.1. Materials and sample preparation

Polycrystalline $CuFeInTe_3$ alloys were synthesized using the melt and anneal technique. The manner in which $CuFeInTe_3$ has been prepared in this work, using the stoichiometry $(CuInTe_2)_{1-x}(FeTe)_x$ with x = 0.5 (see Fig. 1), suggests that Fe-atoms occupy Cu or In crystallographic sites randomly [15,16].

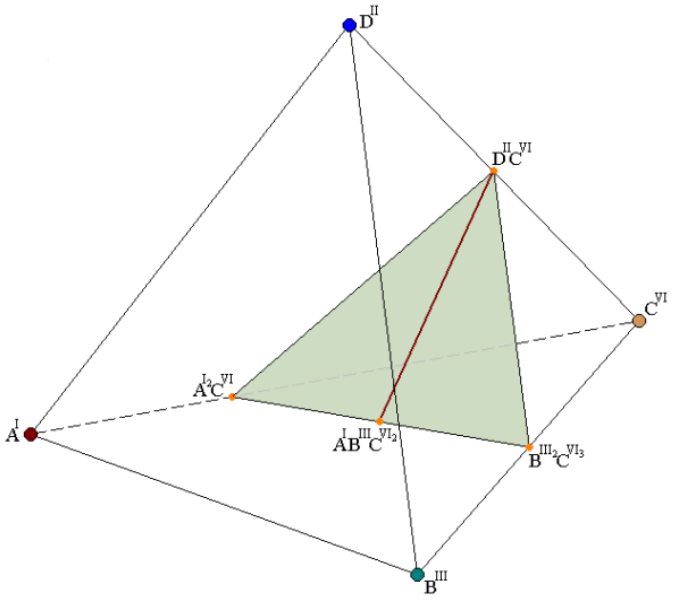

Fig. 1. Representation of the compositional pyramid for A^I-B^{III}-C^{VI}-D^{II} quaternary alloys. The shaded triangle represents the $A^I_2C^{VI}$-$B^{III}_2C^{VI}_3$-$D^{II}C^{VI}$ section whereas the red line is the $(A^I$-B^{III}-$C^{VI}_2)_{1-x}(D^{II}$-$C^{VI})_x$ alloys. For $CuFeInTe_3$: A = Cu, B = In, C = Te, D = Fe and x = 0.5.

Stoichiometric quantities of Cu, Fe, In and Te elements with purity of 99.99% were charged in an evacuated synthetic silica glass ampoule, which was previously subjected to pyrolysis in order to avoid reaction of the starting materials with silica glass. Then, the ampoule was sealed under vacuum ($\sim 10^{-4}$ Torr) and the fusion process was carried out inside a furnace (vertical position) heated up to 1500 K at a rate of 20 K/h, with a stop of 48 h at 722.5 K (melting temperature of Te) in order to maximize the formation of binary species at low temperature and minimize the presence of unreacted Te at high temperatures. The ampoule was shaken by a mechanical system during the entire heating process in order to help completely mix all the elements. When the maximum temperature (1500 K) was achieved, the ampoule was shaken for another 48 hours before cooling at a rate of 20 K/h, until the temperature reached 873 *K*. The ampoule was kept at this temperature for a period of 30 days. Finally, it was cooled to room temperature at a rate of 10 K/h. The color of obtained ingots was bright gray and seemed to be homogeneous. The crystallographic evolution of $(A^I$-B^{III}-$C^{VI}_2)_{1-x}(D^{II}$-$C^{VI})_x$ alloys is as shown in Fig. 2 [18]. The presented example of $(CuInTe_2)_{1-x}(FeTe)_x$ can be extrapolated to any other combinations of A^I, B^{III}, C^{VI} and/or D^{II} atoms. For the x=0.5 composition, a rearrangement of the constituent atoms occurs according to the $P\bar{4}2c$ crystal structure. In principle, a Cu-In-pair must be replaced by 2Fe in such a way that the number of carriers does not change, and the type of electrical conductivity is dictated by intrinsic defects.

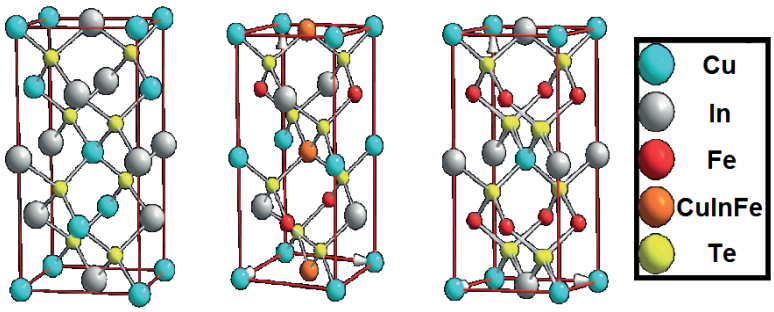

Fig. 2. Evolution of the crystal structure of $(CuInTe_2)_{1-x}$ $(FeTe)_x$ alloys with composition x, at 600 K. Left: x=0, phase α, s.g. $I\bar{4}2d$; center: x=0.5, phase α' s.g. $P\bar{4}2c$; right: x=2/3, phase β', s.g. $I\bar{4}2m$. The orange atom (only in the crystal structure at the center) is labeled as CuInFe because this crystallographic site is shared at random by the three cations Cu, In and Fe [18].

2.2. Characterization techniques

2.2.1. X-Ray Powder Diffraction

A small amount of the sample was thoroughly ground using an agate mortar and pestle and deposited on a zero-background specimen holder. X-ray powder diffraction patterns of the samples were recorded using a PANalytical X'Pert Pro MPD powder X-ray diffractometer operating in Bragg-Brentano geometry using CuK_α radiation with an average wavelength of 1.54187 Å. A tube power of 45 kV and 40 mA was employed. A nickel filter was used in the diffracted beam optics and the data were collected by the X'Celerator one-dimensional silicon strip detector. A ¼° divergent slit, a ½° antiscatter slit, and a 0.02 rad soller slit were set at both the incident and diffracted beams. The scan range was from 5 to 145° 2θ with a step size of 0.008° and a scan speed of 0.0106°/*s*.

2.2.2. Differential Thermal Analysis (DTA)

Phase transition temperatures were obtained from DTA measurements, performed in vacuum in the temperature range of 300 to 1500 K, using a Perkin-Elmer DTA-7. The instrument was calibrated by performing measurements with aluminum and gold as references. The charge was approximately 100-mg of powdered alloy. Both heating and cooling runs were carried out on each sample; the average rates of these runs were approximately 10 K/min. The uncertainty in these temperature determinations was about ±10 *K*. The temperature values of the thermal transitions were obtained, as usual, using the intercept of the base line with the beginning of the corresponding peak.

2.2.3. Optical Diffuse Reflectance Spectroscopy (ODRS)

The optical diffuse reflectance spectrum was obtained using a Varian Cary 5000 UV/VIS/NIR spectrometer equipped with a Harrick Praying Mantis diffuse reflectance accessory that uses elliptical mirrors. The sample was ground and placed into a sample holder to a depth of 3 mm. Barium sulfate (Fisher, 99.92%) was used as a 100% reflectance standard. Data were collected in the range of 2500 to 200 nm at a scan rate of 600 nm/min.

2.2.4. Raman scattering spectroscopy

The Raman spectrum of the $CuFeInTe_3$ sample was obtained by the use of an EZRaman-N (Enwave Optronics) Raman analyzer coupled to the Leica DM300 microscope (with a Leica objective of magnification/numerical aperture ratio 40X/0.65), using an excitation laser source of 532.8 nm output wavelength (~2 mW output power). The spot diameter was about 5 μm.

2.2.5. Hall effect

Room temperature Hall effect measurements were performed in an Ecopia Hall Effect Measurement System (Model HMS-3000)**.** Four electric contacts (soldering In and Sn-paint) were deposited on the sample surface to collect the corresponding I-V curves and measure the ohmic characteristic at room temperature and corresponding electric current.

2.2.6. Seebeck Coefficient

The high temperature Seebeck measurement system is home-built and consists of two Cu blocks against the sample that is pressed in thermal and electrical contact. One block is heated about 5 K above the other and the voltage and temperature difference are monitored as the system returns to equilibrium. The whole system is at a base temperature that can be changed, and we measured the coefficient every 50 K.

2.2.7. Beam Deflection Spectroscopy

The beam deflection (BD) technique used in our measurements is based on the well-established approach [19], using an experimental setup for the transverse BD experiments in its skimming configuration [17, 20]. The sample is periodically heated using a He-Ne laser (632.8 nm 35 mW output power, MELLES GRIOT, Model 25-LHP-928-230), while a quadrant photodiode (RBM - R. Braumann GmbH, Model C30846E) senses vertical deflections of a 543.5 nm (2 mW power) He-Ne laser probe beam (MELLES GRIOT, Model 25-LGR-393-230) propagating parallel and very close to the sample´s surface. These deflections are induced by the spatial periodical variations of the refractive index of the acetonitrile-liquid in contact with the sample's surface, due to the heating. For temperature dependent measurements, the sample's absolute temperature is changed using a controlled heating system based in Peltier elements. The dependences of the signal amplitude and phase on the modulation frequency of temperature oscillations, *f,* induced in the fluid above the examined sample, were collected. To determine the thermal conductivity of the examined sample the least-squares fitting procedure of the theoretical curves to both the amplitude and phase of the experimental data was carried out using the model based on complex geometrical optics equation, as described in detail elsewhere [20].

3. Results and discussions

3.1. X-ray powder diffraction (XRPD)

The XRPD pattern of $CuFeInTe_3$ is shown in Fig. 3. The indexation results in a tetragonal phase with lattice parameters a=6.186±0.002 Å and c=12.428±0.002 Å (c/a=2.009), that are slightly larger than those of the ternary $CuInTe_2$ (a=6.179 Å, c=12.36 Å, c/a= 2.000 [12]). The partial substitution of Cu^{1+} and In^{3+} by Fe^{2+}, as represented in Fig. 2, would induce a lattice contraction because of the smaller size of Fe^{2+}; however, a contrary effect is observed. This fact suggests the presence of interstitial Fe^{2+}, in addition to the described Cu^{1+} and In^{3+} substitutions [18], in the $CuFeInTe_3$ lattice, probably due to limitations in Fe^{2+} solubility for such relatively high concentration. This hypothesis is supported by the fact that $Fe_{1.125}Te$ traces were found in the powder diffraction pattern of $CuFeInTe_3$ (marked with asterisks in Figure 3). The presence of this impurity related to the atomic stoichiometry used in the synthesis procedure (Cu:Fe:In:3Te), also indicates a probable Te and Fe deficiency in $CuFeInTe_3$ structure.

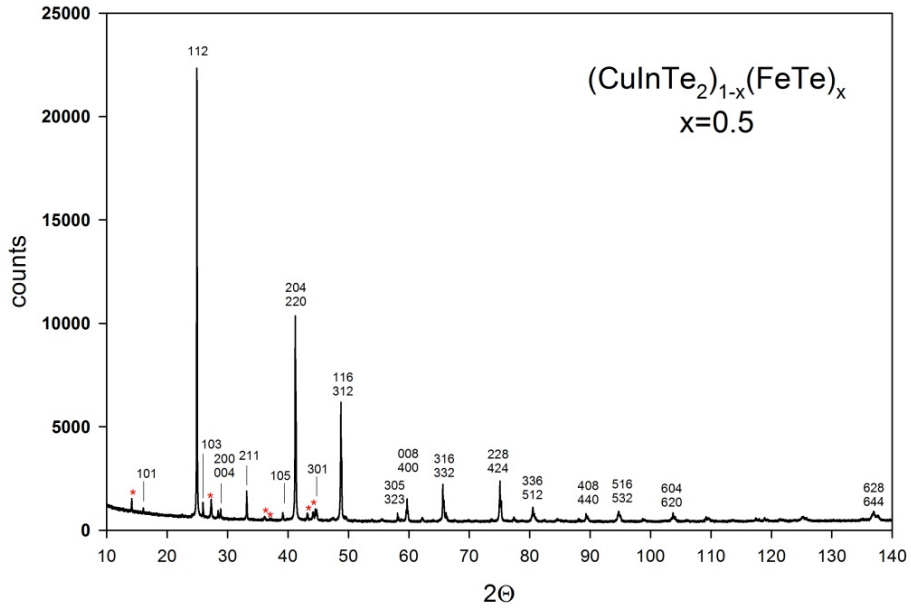

Fig. 3. X-ray powder diffraction pattern of the alloy $CuFeInTe_3$. The labels are the respective hkl-Miller indices and the asterisks signal traces of a secondary phase identified as $Fe_{1.125}$ Te.

3.2. Differential Thermal Analysis (DTA)

In Fig. 4 the DTA thermogram of $CuFeInTe_3$ is presented. In the heating cycle, there are observed two peaks: the first one, at 928 K corresponds to the order-disorder phase transition temperature (T_{o-d}) from the chalcopyrite crystal structure to a semi-ordered chalcopyrite, while the second one at 990 K is the melting point (M_p). These values are close to those reported for $CuInTe_2$ (M_p = 1062 *K* and T_{o-d} = 945 K [15]); but, the decrease of the melting point (150 K) with composition is clear.

In the cooling cycle, three peaks are clearly seen: the first one corresponds to a liquid to solid+liquid transition, the second one to a solid+liquid to solid transition and the third one to the order-disorder transition. The thermogram indicates an incongruent melting (and solidification) point clearly being observed in the cooling cycle (but not in the heating). This apparent incongruency between heating and cooling curves may be possible due to the results of overcooling (or overheating) effects, which are sometimes observed in this technique, despite the fact that the heating and cooling rates are almost identical. In $CuInTe_2$ the solid+liquid region between the liquid and the sphalerite phase is relatively narrow; whereas for $CuFeInTe_3$, the cooling curve suggests that this region is wider. We are preparing several samples in the $(CuInTe_2)_{1-x}(FeTe)_x$ and a phase diagram will be proposed soon.

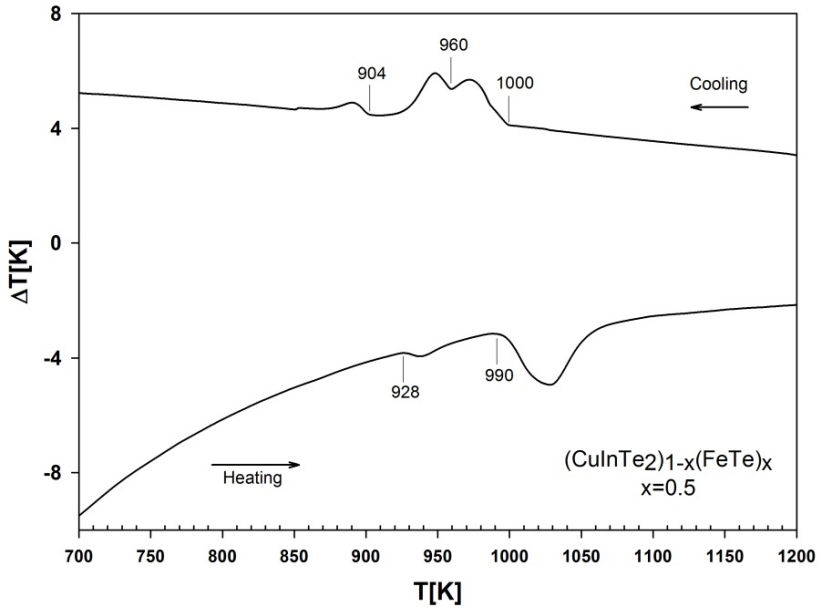

Fig. 4. DTA thermogram of the alloy $CuFeInTe_3$. The labels indicate the transition temperatures for the heating (bottom curve) and cooling (top curve) cycles.

3.3. Optical Diffuse Reflectance Spectroscopy (ODRS)

The diffuse reflectance spectrum was converted to absorption spectrum using the Kubelka-Munk function ($F(R)$) [21] for the $CuFeInTe_3$ sample is shown in Fig. 5a. It is noteworthy that in the energy range around 0.6-0.9 eV the spectral shape is clearly different from that typically observed for $CuInTe_2$, where almost no absorption occurs [22]. Considering the fact that the FeTe impurity has its band-gap in the UV-vis region [23], the mentioned feature indicates a different electronic band structure for $CuFeInTe_3$, with respect to that of $CuInTe_2$, that is determined by the relatively high content of Fe^{2+} atoms inserted in the crystal lattice. An indirect band-gap of 0.60 eV and a direct band-gap of 0.91 eV were found from Tauc´s plots [24, 25], presented in Figure 5b. Although the band-gap dependence on chemical composition for some of the $CuInTe_2$-based alloys, such as $Zn_{2x}(CuIn)_{1-x}Te_2$ is rather well known [22], such information for the $CuFeInTe_3$ material is not available. Additionally, no previous experimental or theoretical reports about an indirect transition, in addition to a direct one, for any $CuFeInTe_3$-based alloys, has been reported in the literature. No significant Urbach tails were found in this spectrum.

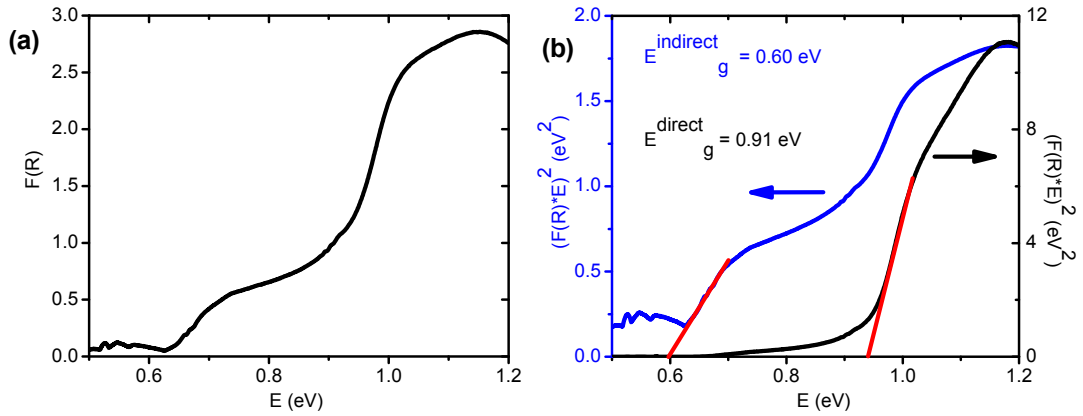

Fig. 5. (a) Kubelka-Munk function of the $CuFeInTe_3$ alloy, computed from the corresponding diffuse reflectance UV−VIS−NIR spectrum a (blue curve). (b) Plots for indirect and direct band gap calculations.

3.4. Raman scattering analysis

The Raman scattering spectrum of the $CuFeInTe_3$ sample is presented in Fig. 6; two peaks are observed. The first and most intense peak is located at 128 cm^{-1}, while the other less intense at 185 cm^{-1}. There is no theoretical or experimental information available in the literature related to Raman scattering in $CuFeInTe_3$ that can be used for comparison with our result. However, $CuInTe_2$, which has a similar structure, has its most intense Raman signal at 127 cm^{-1}, which has been assigned to an A_1 mode that arises due to the in-plane motion of tellurium atoms with the cations at rest [26]. Additionally, a peak at 182 cm^{-1} has been assigned to a longitudinal optical E mode in $CuInTe_2$ [26]. Because of the similarity of these materials (see Figure 2), it seems to be reasonable to extrapolate the mentioned interpretation to $CuFeInTe_3$. No other signals were detected in the explored spectral range for $CuFeInTe_3$, which is different from the typical Raman spectrum of $CuInTe_2$ [26]. We hypothesize, that the Fe incorporation, in a relatively high concentration, into the $CuFeInTe_3$ alloy lattice has particularly affected the phonon dispersion branches related to the modes that are present in the case of the $CuInTe_2$ counterpart but not observed here.

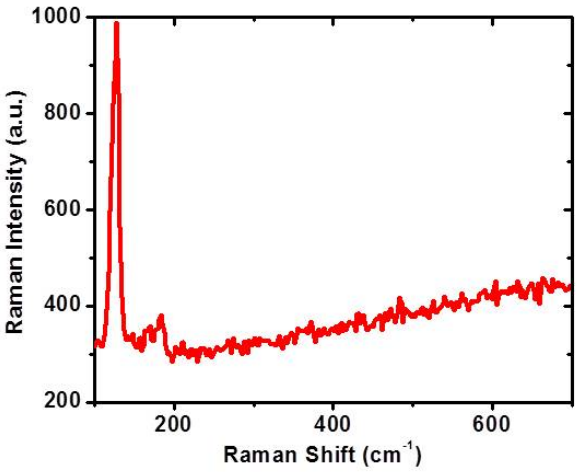

Fig. 6. The Raman spectrum of the $CuFeInTe_3$ sample (P_{exc}=2 mW, λ_{exc}=532.8 nm).

3.5. Hall effect measurements

By performing the Hall measurements, the charge carrier concentration (n), mobility (μ), resistivity (ρ), and electrical conductivity (σ) of $CuFeInTe_3$ were found at room temperature (Table I).

I [mA]	n [10^{19} cm^{-3}]	μ [cm^2/V s]	ρ [$10^{-2}\Omega$cm]	σ [$\Omega^{-1}cm^{-1}$]
1	-8.12	6.62	1.16	86.21

Table I. Hall effect measurements at ambient temperature.

Here, the conductivity of $CuFeInTe_3$ was found to be n-type (n=10^{19} cm^{-3}), which is in contrast with the typical p-type conductivity of $CuInTe_2$ with a hole concentration higher than 10^{17} cm^{-1} [12]. For $CuInTe_2$, the usually p-type conductivity has been attributed to In_{Cu} antisite defects and anion vacancies, V_{Te} [27]. It is important to mention that the usually believed acceptor character of V_{Te} in $CuInTe_2$ [27] strongly contrasts with the well-known capability of this type of vacancy for introducing shallow levels to the conduction band in others chalcogenides [28-31]. In the case of $CuFeInTe_3$, the substitution of Cu^{1+} by the higher valence cation Fe^{2+}, leaving a weakly bound electron, can result in an n-type doping. Additionally, the possible presence of Te^{2-} vacancies (as previously discussed in the XRD section) could also acts as electron donor centers, as for other chalcogenides [28-31]. The electron mobility of the $CuFeInTe_3$ sample (6 cm^2/Vs at 300 K) is much smaller than that observed for the holes in $CuInTe_2$ (105 cm^2/V s) [12]. Collectively, the charge carrier concentration and their mobility result in a much lower resistivity for $CuFeInTe_3$ (1.16x$10^{-2}\Omega$cm), on the order of metals, with respect to that of $CuInTe_2$ (14 Ωcm) [12].

3.6. Seebeck coefficient and electrical conductivity as a function of temperature

Measurements of the electrical conductivity and Seebeck coefficient were performed for the temperature range of 300-450 K. In Fig. 7a, the electrical conductivity of $CuFeInTe_3$ as a function of temperature T is presented. It is seen, that σ decreases with increasing temperature T. It can be noticed, that $d\sigma/dT<0$, which indicates metallic behavior of the conductivity and further that the material is a degenerate semiconductor with a high, nearly temperature independent carrier concentration. In such a case, the temperature dependence of the carrier mobility, related to the increase in phonon concentration, is responsible for the negative slope of $\sigma(T)$. Similarly $d\sigma/dT<0$ is also observed for other diamond-like materials. For example, a decrease in electrical conductivity as a function of temperature is observed for all $Cu_2Sn_{1-x}In_xSe_3$ samples where $x>0$ [32]. In the case of Mn-doped $CuInSe_2$; however, the degenerate semiconductor behavior is not observed until the temperature reaches ~ 425 °C [33].

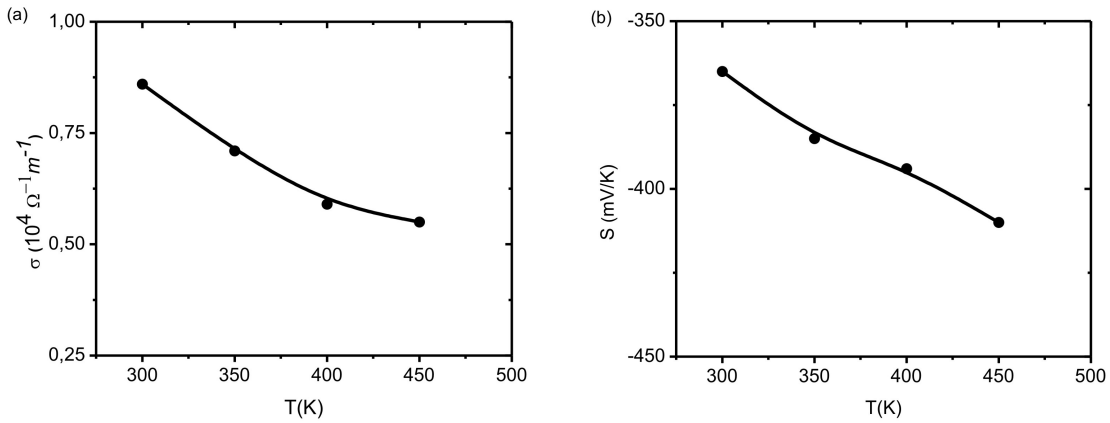

Fig. 7. Temperature dependence of (a) electrical conductivity and (b) Sebeeck coefficient for $CuFeInTe_3$.

In Fig. 7b, the Sebeeck coefficient (S) as a function of temperature is plotted. The almost linear increase of the Seebeck coefficient is typical for metals and degenerate semiconductors [34]. The negative value of the Seebeck coefficient confirms the n-type conductivity of $CuFeInTe_3$. The large negative value of the Sebeeck coefficient achieved (S=-375 μV/K) at room temperature is related to the strong coupling between carriers and the spins of magnetic ions as it is for magnetic semiconductors such as $CuFeInTe_3$ [35]. This strong interaction may lead to a large effective mass of carriers, which can enhance the Seebeck coefficient and provides high carrier conduction. For metals or degenerate semiconductors (parabolic band, energy-independent scattering approximation) the Seebeck coefficient is given by [36]:

$$S = \frac{8\pi^2 k_B^2}{3eh^2} m^* T \left(\frac{\pi}{3n}\right)^{2/3}, \qquad (2)$$

where n is the carrier concentration, k_B the Boltzmann constant, h is Planck's the constant, and m^* is the effective mass of the carrier. These results show, that alloying $CuInTe_3$ with

Fe^{2+} results in large Seebeck coefficient, which indicates an increased carrier effective mass.

3.7. Thermal conductivity and thermoelectric figure of merit determination

In Fig. 8a the temperature dependence of the thermal conductivity, κ, is shown. It can be noticed that κ decreases with the increase in *T*. Such a behavior is typical for metallic or degenerate semiconductor materials. The value of κ at room temperature, 4.8 W/Km, is lower than that observed for $CuInTe_2$ at 300 K [12]. The polycrystalline character of the $CuFeInTe_3$ sample and the structural features induced by the inclusion of Fe^{2+} atoms in the lattice, as well as the impurity phase present, as discussed above, produce scattering of phonons and affect the thermal properties by diminishing the value of the thermal conductivity to k =4.8 W/mK (300 K) compared to that of $CuInTe_2$ (κ =6 W/mK). In general the thermal conductivity consists of two parts and in semiconductors both have to be considered. An electronic contribution, κ_e, which increases with increasing temperature and the lattice contribution, κ_L, which decreases with increasing temperature via the phonons dominated by the lattice vibrations ($\kappa=\kappa_e+\kappa_L$). The electronic part of the thermal conductivity is related to the electronic conductivity via the Wiedemann-Franz law ($\kappa_e=L\sigma T=Ln\mu T$). By expressing the thermal conductivity as the sum of its two components κ_e and κ_L and applying the Wiedemann-Franz law, the figure of merit (Eq.1) can be written as:

$$zT = \frac{\sigma S^2 T}{\kappa} = \frac{S^2 / L}{1 + \frac{\kappa_l}{\kappa_e}}, \qquad (3)$$

where L is the Lorentz factor, that is 2.4×10^{-8} J^2 K^{-2} C^{-2} for free electrons. It is seen from Eq. 3 that to optimize zT, the reduction of the phonon contribution to the thermal conductivity is required. In our case, the phonon scattering depressed κ to a value of 4.8 W/mK and did not affect σ so much, which in combination with high S allowed the enhancement of the figure of merit up to zT=0.075 at room temperature compared to zT=0.028 for $CuInTe_2$ [8] and zT=0.06 for $CuFeS_2$ [34].

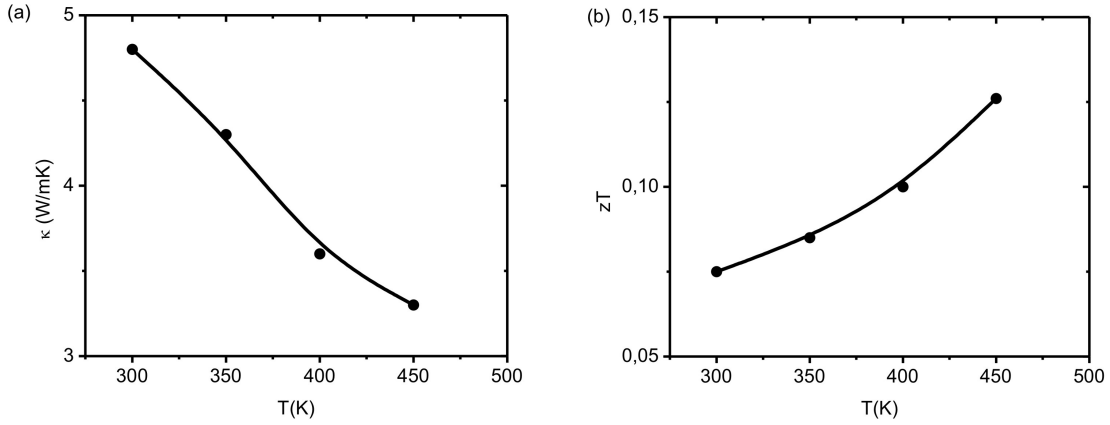

Fig. 8. Temperature dependence of (a) thermal conductivity κ and (b) the thermoelectric figure of merit, zT.

The thermal conductivity, as shown in Fig. 8a, decreases rapidly with rising temperature as a result of the stronger phonon-phonon scattering (especially the Umklapp processes) at higher temperatures. By comparison to Mn-substituted $CuInSe_2$, which displays similar behavior and magnitude of the thermal conductivity, the value for κ would likely dip well below 2 μV/K at temperatures above 500 K [33]. The thermal conductivity of the chalcopyrite system can be further reduced by appropriate inclusion of secondary phases as phonon dispersion centers. Alternatively, doping or introduction of vacancies could serve to further decrease the thermal conductivity. For example, in the $Ag_{1-x}InTe_2$ system a simultaneous increase in the electrical conductivity and decrease in the thermal conductivity is observed such that an enhanced zT is attained where x>0 and the maximum zT is found for the x=0.5 sample [37].

In Fig. 8b, *zT* is plotted against T. The *zT* values reach ~0.126 at 450 K, though they keep increasing with *T*, and much higher values are expected for higher values of *T*. At 450 K, the *zT* of the title material is much larger than that observed for several other chalcopyrites and the corresponding substituted systems, i.e. $CuFeS_2$ [38], Fe-substituted $CuInS_2$ [39], Mn-substituted $CuInSe_2$ [33], $AgInSe_2$ [40], and $Ag_{1-x}InTe_2$ [37]. Furthermore, since the zT of $CuFeInTe_3$ increases with increasing temperature from room temperature to 450 K, much higher values are expected for higher values of *T*. Interestingly, the *zT* for $CuFeInTe_3$ at 450 K rivals that of $CuGaTe_2$ which reaches a *zT* of 1.4 at 950 K [41].

4. Conclusions

It was demonstrated in this work, that $CuFeInTe_3$ is a promising n-type TE material applicable at high temperatures. Both crystal structure as well as electronic structure are altered by the inclusion of Fe^{2+} ions in the $CuFeInTe_3$ alloy as evidence by both a direct and indirect bandgap found for $CuFeInTe_3$. Iron incorporation does not significantly alter the electrical conductivity but the modified structure and composition allow for a significant decrease in the thermal conductivity. As a result, the *zT* value of $CuFeInTe_2$ reaches 0.126 at 450 K, which is better than the value obtained in the case of $CuInTe_2$ and similar to the value of the n-type, doped $CuFeS_2$ semiconductor. Collectively these results suggest, that these magnetic semiconductors could be good thermoelectric materials, which could be still

improved by further optimization of the atomic composition and/or by the appropriate inclusion of additional secondary phases. Additionally, further doping with the proper substituent could result in a simultaneous increase in the electrical conductivity and a favorable decrease in the thermal conductivity as observed in other diamond-like systems [33, 42].

Acknowledgments

The authors gratefully acknowledge the financial support received from CLAF-CECITIDF (project 073/2013)**,** CONACyT grant 264093, CDCHTA for grant code C-1885-14-05-B, FONACIT grant (PEII N°1697), ICTP through the Research Associateship Program and SPIE-ICTP Anchor Research Laboratory. We also thanks for grants from SIP-IPN (1491 and 1638), CONACyT (205640 and 2011-01-174247). The support from COFAA-IPN through the SIBE Program is also acknowledged. JAA, JAB and JHZ acknowledge support from the National Science Foundation under grant no. DMR-1201729. I.Z-D acknowledges postdoctoral fellow from CONACyT project number 174247 (Desarrollo de Materiales para Tecnologías de Energías Renovables).

References

[1] D. M. Rowe, CRC Handbook of Thermoelectrics (CRC Press, Boca Raton, 1995).
[2] G.J. Snyder, E.S. Toberer, Nat. Mater. 7 (2008) 105-114.
[3] A.I. Hochbaum, R. Chen, R.D. Delgado, W. Liang, E.C. Garnett, M. Najaria, A. Majumdarand P. Yang, Nature 451 (2008) 163-167.
[4] K. Biswas, J. He, I. D. Blum, C. Wu, T. P. Hogan, D. N. Seidman, V. P. Dravid, M. G. Kanatzidis, Nature 489 (2012) 414-418.
[5] B. C. Sales, D. Mandrus, R. K. Williams, Science 272 (1996) 1325-1328.
[6] Y. Pei, H. Wang, G. J. Snyder, Adv. Mater. 24 (2012) 6125-6135.
[7] Y. He, T. Day, T. S. Zhang, H. L. Liu, X. Shi, L. D. Chen, G. J. Snyder, Adv. Mater. 26 (2014) 3974-3978.
[8] D. R. Brown, T. Day, K. A. Borup, S. Christensen, B. B. Iversen, G. J. Snyder, APL. Mat. 1 (2013) 52107.
[9] H. Kleinke, Chem. Mater. 22 (2010) 604-611.
[10] T. Plirdpring, K. Kurosaki, A. Kosuga, T. Day, S. Firdosy, V. Ravi, G.J. Snyder, A. Harnwunggmoung, T. Sugahara, Y. Ohishi, H. Muta, S. Yamanaka, Adv. Mater. 24 (2012) 3622-3626.
[11] P. Prabukanthan, R. Dhanasekaran, Mater. Res. Bull. 43 (2008) 1996-2004.
[12] R. Liu, L. Xi,H. Liu,X. Shi, W. Zhang, Chem. Commun. 48 (2012) 3818-3820
[13] N. Cheng, R. Liu, S. Bai, X. Shi, L. Chen. J. Appl. Phys. 115 (2014) 1637051-1637057.
[14] J.Yang, S. Chen, Z. Du, X. Liu, J. Cui. Dalton Trans.43 (2014)15228-15236.
[15] P. Grima-Gallardo, K. Cardenas, M. Quintero, J. Ruiz. Adv. Mater. Sci. Technol. 2 (2000) 1-5.
[16] P. Grima-Gallardo, F. Alvarado, M. Muñoz, S. Durán, M. Quintero, L. Nieves, E. Quintero, R. Tovar, M. Morocoima, M.A. Ramos. Phys. Status Solidi 209 (2012) 1141–1143.
[17] D. Korte, H. Cabrera, P. Grima, M. Franko, Submitted Int J. Therm. Sc. (2015).
[18] P. Grima-Gallardo, S. Torres, M. Quintero, L. Nieves, E. Moreno, G.E. Delgado. J. Alloys Compd. 630 (2015) 146-150.
[19] A. C. Boccara, D. Fournier, J. Badoz, Appl. Phys. Lett. 36 (1980) 130-132.
[20] D. Korte, M.Franko. Josa. A, 32 (2015) 61-74.
[21] P. Kubelka. JOSA 38 (1948) 448-457.
[22] S. Schorr V. Riede, D. Spemann, T. Doering. J. Alloys Compd. 414 (2006) 26–30.
[23] K. B. Messaoud, A. Gantassi, H. Essaidi, J. Ouerfelli, A. Colantoni, K. Boubaker, M. Amlouk. Adv. Mat. Sc. Eng. 2014 (2014) 1-6.
[24] J. Tauc. MRS Bull. 3 (1968) 37−46.
[25] O. Schevciw, B. William, White Mat. Res. Bull. 18 (1983) 1059-1068.
[26] M R Ananthan, Bhaskar Chandra Mohanty, S Kasiviswanathan, Semicond. Sci. Technol. 24 (2009) 075019-075026.
[27] G. Marín, S.M. Wassim, G. Sánchez Pérez, P. Bocaranda, A.E. Mora. J. Elect. Mater. 27 (1998) 1351-1357.

[28] L. E. Oikkonen, M. G. Ganchenkova, A P Seitsonen, R M Nieminen, J. Phys.: Condens. Matter 23 (2011) 422202-422207.
[29] S. Niki, R. Suzuki, S. Ishibashi, T. Ohdaira, P.J. Fons, A. Yamada, H. Oyanagi, T. Wada, R. Kimura, T. Nakada, Thin Solid Films 387 (2001) 129-134.
[30] A. Jagomagi, J. Krustoka, J. Raudojaa, M. Grossberga, M. Danilsona, M. Yakushev, Phys. B 337 (2003) 369–374.
[31] J. C. Nickerson, R. M. White, K. N. Lee, R. Bachmann, T. H. Geballe, G. W. Hull, Phys. Rev. B. 3 (1971) 2030-2041.
[32] X. Shi, L. Xi, J. Fan, W. Zhang, L. Chen, Chem. Mater. 22 (2010) 6029-6031.
[33] J. Yao, N. J. Takas, M. L. Schliefert, D. S. Paprocki, P. E. R. Blanchard, H. Gou, A. Mar, C. L. Exstrom, S. A. Darveau, P. F. P. Poudeu, J. A. Aitken, Phys. Rev. B, 84 (2011) 075203.
[34] Y. Li,T. Zhang,Y. Qin,T. Day, G. J. Snyder, X. Shi, L. Chen. J. App. Phys. 116 (2014) 2037051-2037058.
[35] N. Tsujii, T. Mori, Appl. Phys. Exp. 6 (2013) 043001-043001.
[36] M. Cutler, J. F. Leavy, R. L. Fitzpatrick, Phys. Rev. 133 (1964) A1143–A1152.
[37] Y. Aikebaier, K. Kurosaki, T. Sugahara, Y. Ohishi, H. Muta, S. Yamanaka, Mat. Sci Eng. B 177 (2012) 999-1002.
[38] N. Tsujii, J. Electron. Mater. 42 (2013) 1974-1977.
[39] Burnett, D. Johanna, X. Tianhong, M. Sorescu, B. R. Strohmeier, J. Sturgeon, O. Gourdon, K. Baroudi, J. Yao, J. A. Aitken, J. Sol. St. Chem. 197 (2013) 279-87.
[40] P. Z. Ying, H. Zhou, Y. L. Gao, Y.Y. Li, Y. P. Li, X. L. Liu, J. L. Cu. K. Eng. Mater. 519 (2012) 188-192.
[41] T. Plirdpring, K. Kurosaki, A. Kosuga, T. Day, S. Firdosy, V. Ravi, G. j. Snyder, A. Harnwunggmoung, T. Sugahara, Y. Ohishi, H. Muta, S. Yamanaka, Adv. Mater. 24 (2012) 3622-3626.
[42] J. D. Burnett, O. Gourdon, K. G. S. Ranmohotti, N. J. Takas, H. Djieutedjeu, P. F. P. Poudeu, J. A. Aitken, Mat. Chem. Phys. 147 (2014) 17-27.

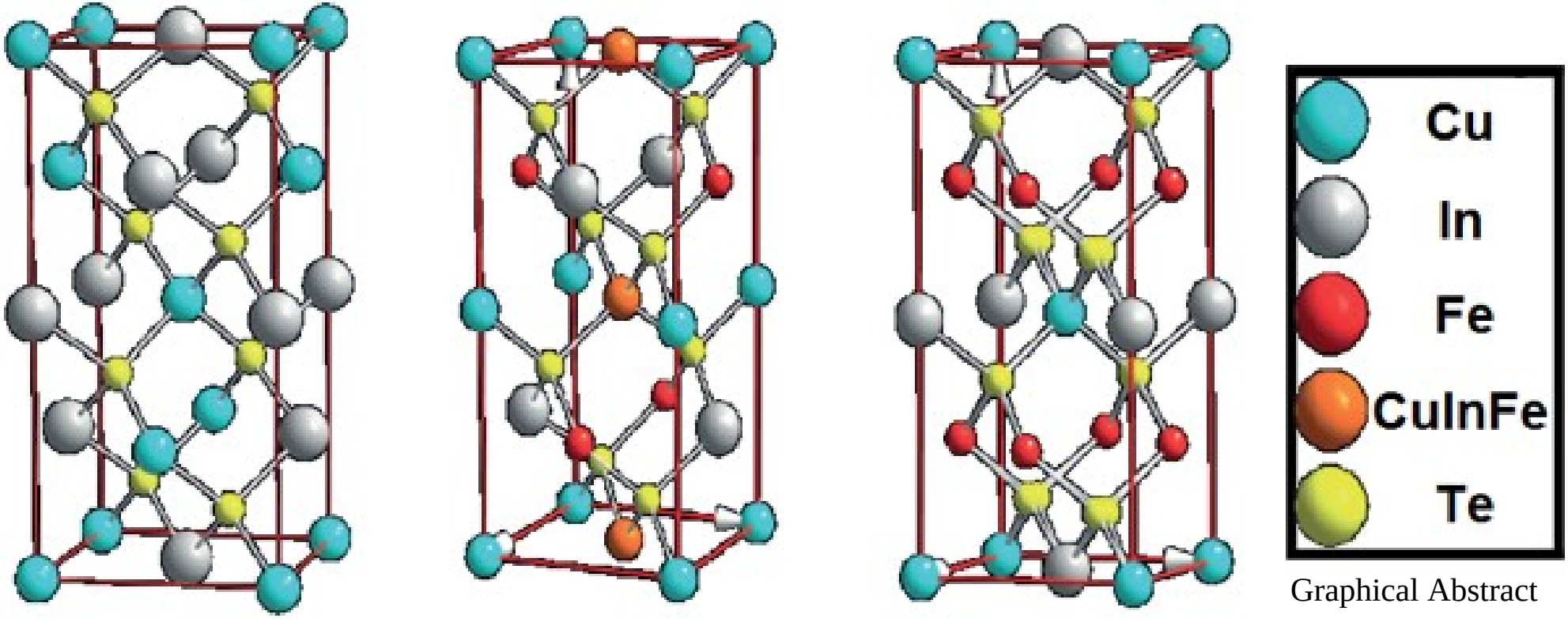

Graphical Abstract